Chapter 16

Recent Advances in Mechanical Properties of Nanowires

Hui Li and Fengwei Sun

Additional information is available at the end of the chapter

http://dx.doi.org/10.5772/ 52592

1. Introduction

Over the recent decade, nanowires (NWs) have attracted great attention due to their small size and thus large surface area to volume ratio which results in interesting surface effect. As the devices become smaller and smaller, NWs serve as basic building blocks for future electronic and electromechanical systems, such as performing sensitive mass and force detection, acting as high frequency resonators and so on. The potential of NWs in future application has led to significant interest in experimental and theoretical characterization of the size-dependent properties of NWs. Constructing and determining NWs with better mechanical properties than the corresponding bulk materials are a challenge even though the technical equipments are improving. Meantime, another important thing is how to integrate NWs with the existing technology. Material simulations of investigating mechanical properties of NWs are still an important technique until now. This is essential to understand the inherent mechanism of the NWs' deformation. The deformation mechanism depends on several aspects including the intrinsic material properties, crystal structures, surface geometry, applied stress state, axial and surface orientation and exposed transverse surfaces. Until now many experimental techniques have been utilized to investigate mechanical properties. Scanning tunneling microscope (STM) was employed to study atomic contact of NWs and their conductance [1-3] in early experiments. Since a novel nanobridge structure of Au NWs is generated by electron-beam irradiation on a thin Au film in an ultrahigh vacuum transmission electron microscope (TEM) [4], many researches have been carried out to study the properties of this stable structure. A specific developed STM supplemented with a force sensor is used in order to reveal the process of forming thin Au NWs [5]. Atomic force microscope(AFM) has also attracted particular attention due to its high spatial resolution and force-sensing capabilities[6] and was used for bending tests of single crystal, micromachined

silicon beams[7]. Recently developed in situ TEM technique can also be applied to perform bending deformation of single SiC NWs[8]. Theoretically, some new simulation methods are developed and widely used to study nanoscale materials. For FCC crystal metal NW, most simulations were performed with embedded atom method (EAM) [9-17], which reproduce exactly the experimental second-order and third-order elastic moduli as well as the phase stability. Furthermore, the modified EAM with the developed potential [18-20] is utilized to study the phase transformation of Au NWs. While for the semiconductor NWs, Tersoff many-body bond-order reactive potential and Stillinger-Weber many-body potential [21, 22] are appropriate to describe interatomic interactions[23] in Si and SiC NW. Tight-binding molecular dynamics simulations [24-26], which lies in between first principles and empirical methods is also used to study the atomic structure of Au NW. It is more accurate than empirical potential methods because it explicitly includes the electronic structure, and is much faster than first principles methods.

This review is organized as follows. In section 2, we discuss some novel mechanical properties of single crystal metal NWs caused by surface effect, strain rate, temperature and so on. In section 3, we consider the mechanical properties of semiconductor NWs such as Si, Si compound and ZnO et. al. In section 4, some other irregular structures of NWs are investigated to compare the mechanical properties with bulk and normal crystal NWs. In the last section, we discuss the enhancement of NWs which are encapsulated in carbon nanotubes during compression.

2. Single crystal metal nanowires

2.1. Side surface effect on axial deformation mode

Several researchers have demonstrated that the structures and properties of nanomaterials can be quite different from those of bulk materials by experiments or molecular dynamics (MD) simulations due to surface effect which results in different deformation modes.

In compression of the <110> NW, low energy {111} side surfaces prevented free-surface initiated slip. On the contrary, slip is observed for higher energy {100} and {110} side surfaces. For the <100> wires, distributed stacking faults appearing in the <100>/{110} wires result from simple and important rotation of the crystal orientation along its longitudinal axis, which is different from the deformation mode of twinning for the <100>/{100} wires. Some other important findings of fundamental deformation mechanism are revealed in Ref.[27].

2.2. Size effect on Young's modulus

Mechanical properties based on Au NW bending under the lateral load from an AFM tip are performed by Wu et.al [6]. Their experiments reveals that Young's modulus is essentially independent of diameter, whereas the yield strength is largest for the smallest diameter wires, with strengths up to 100 times that of bulk materials, and substantially larger than that reported for bulk nanocrystalline metals. MD simulations demonstrate that Young's modulus

is independent of strain rate and cross sectional size of specimen. Neither geometry nor surface structure has an appreciable effect on the modulus[28]. However, in some other molecular statics simulations[29], the modulus values for NWs with a <110> axial orientation are observed to increase with decreasing cross-sectional thickness, while for NWs with a <100> axial orientation the modulus values decrease with decreasing cross-sectional thickness. This is attributed to the nonlinear elasticity of the NW core and dissimilar surface and core elastic modulus values[12]. The size-dependence modulus[28] is consistent with predictions based on core nonlinear elasticity, but it is difficult to separate the surface elasticity and core nonlinearity effects because of a lack of strong trends with NW size or surface orientation[29]. Meantime, deformation induced by surface stresses might also has a significant impact on the Young's modulus in bending simulations, where a strong boundary-condition dependence is also found [30]. Therefore, a nonlinear, finite deformation formulation [30] that captures changes in both bulk and surface elastic properties resulting from surface stress-induced deformation is critical to reproducing the experimentally observed boundary-condition dependence in Young's modulus of metal NWs.

2.3. Surface stress effect

2.3.1. Surface stress effects on the resonant properties

Boundary conditions determine how the NWs deform in response to surface stresses. Fixed/free NWs (cantilever) are able to contract, thus relieving the tensile surface stresses, and leading to a state of compression in the NW core. Fixed/fixed NWs are constrained such that they cannot deform axially, causing them to exist in a state of tensile stress.

The reduction in resonant frequencies for the fixed/free boundary condition and increase in resonant frequencies for the fixed/fixed boundary condition [31] indicate that those NWs are expected to be elastically softer, and stiffer, respectively, than the corresponding bulk material, agreeing with recent experimental results for both free-standing[32], and fixed/fixed NWs [33-35]. The variation in NW resonant frequencies due to surface stresses was found to be dependent on the NW aspect ratio. In contrast, no dependence of the resonant frequencies on the surface area to volume ratio was found, again agreeing with recent experimental data [36]. The variation in resonant frequency for the fixed/free case occurs due to the fact the bulk <100> material softens under compression. Therefore, the resonant frequencies of fixed/free NWs with other orientations that stiffen under compression, such as <110>, are expected to increase rather than decrease as compared to the corresponding bulk material. In the higher order resonant modes (second bending, stretch, twist), surface stresses cause the largest variation in the second bending frequencies, while the twist and stretch frequencies show little variation due to surface stresses. All higher order resonant frequencies decrease with respect to the fundamental bending frequency with increasing aspect ratio for fixed/fixed NWs due to surface stresses, while the higher order resonant frequencies increase with respect to the fundamental bending frequency for fixed/free NWs[31].

2.3.2. Surface stress induced phase transformation

Surface-stress-induced phase transformation in Au NWs is an interesting phenomenon. The emergence of the transformation is dominated by wire size, initial orientation, boundary conditions, temperature and initial cross sectional shape. For a crystal with <100> axial orientation, surface stresses alone cause Au NWs with cross-sectional area below 4 nm^2 to transform from a FCC structure to a body centered-tetragonal (BCT) structure [20]. Not only has this transformation appeared in Au NWs, but also in alloy NWs. Park has demonstrated that B2 NiAl NWs undergo a stress-induced martensitic phase transformation to a BCT phase as well by the propagation and annihilation of {101} twinning planes [37]. While for Au NWs formed along the [110] direction, quantum mechanical molecular dynamics shows that it reconstructs upon stress to form helical NWs [38]. The different final structures are probably due to temperature effect as well. The helical NW is obtained by annealing the crystal structure from 600K, while the BCT structure is relaxed to a minimum energy state at 0K with conjugate gradient method.

Some further simulations have also been performed [39] to investigate the core/shell structure in which the crystalline core is encapsulated by a glassy shell. Such core/shell heterostructures usually possess particularly attractive applications in the nanoelectromechanical system, owing to their high complexity and functionality. The elongation of the metallic NW is realized by moving the rigid atoms at one end along the axial axis. The rigid atoms are stretched 0.001nm every 1 ps. This strain rate is sufficient to dissipate excess energy to maintain a constant temperature. The Berendsen method [40] is used to control the system temperature. The motion equations are solved by a fourth-order Nordsieck-Gear predictor corrector method[41] using a time step of 1 fs. The average of the virial stress component along the axial axis during deformation is taken as the macroscopic stress of the wire. This stress measure totally differs from either engineering stress or true stress, which has been used widely in molecular simulations [42-44]. Here the low temperature (T=50K) was used to highlight the material responses upon mechanical activation, as the simulated quenching glass structure after rapid cooling is usually more prone to thermal activations than the experimental one. Continuous deformation with noticeable necking occurs to the core/shell NW instead of discrete displacement as shown in Fig.1.

The core/shell structure, which can even be spun into a single atomic chain, tends to display much larger plasticity than the crystalline one. Most importantly, during elongation, local amorphization happens in the high strained region. Generally, it is thought that the amorphization behavior in nanoscale materials is induced by the high strain rate or the entropy at a high temperature. In terms of our simulation, the strain rate of 0.006% ps^{-1} for a 16.3nm long NW, which is equivalent to an approximate stretch velocity of 1.0ms^{-1}, belongs to the range of low stretch velocity compared with previous simulation results. Therefore, we suggest that the surface amorphous layer would induce the disorder of the crystalline core during the elongating process.

http://dx.doi.org/10.5772/ 52592

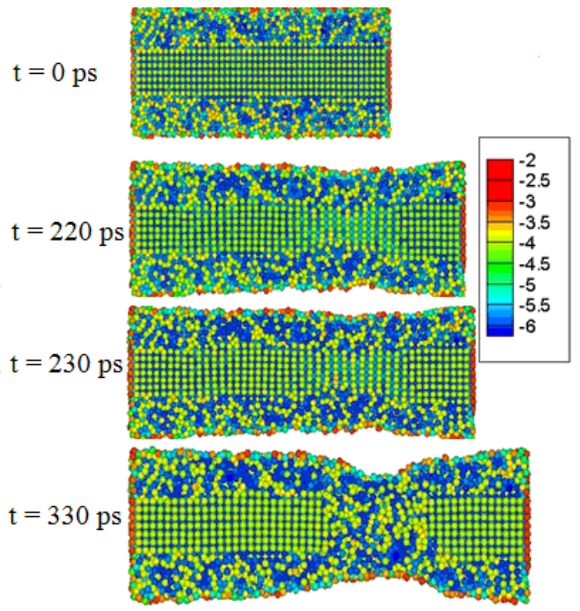

Figure 1. The stretching process of core-shelled CuZr NW, the color bar is to illustrate the contour plots of the per-atom potential energy.

To shed light on the elastic and plastic deformation mechanism in the core/shell NW, evolutions of energy and structure in three key deformation stages are provided in Fig. 2. Here, E_{per} is the total energy per atom at different stretching moment. For the sake of simplicity, an original B2 unit cell taken from the denoted region is used to track the structural transformation. Figure 2(a) shows an initial cross-section image along the axial direction. Figure 2(b) shows an incipient elongating stage. Initially, the original B2 lattice in crystalline core is cubic with a lattice parameter of 0.361 nm. When the stress is applied, a typical martensitic transformation from B2 to BCT phase is observed. That is, a set of new lattice parameters of a=0.289nm and c=0.393nm forms in the crystalline-core zone. When further elongated as shown in Fig. 2(c), the lattice in the deformed crystalline core exhibits increasingly serious distortion. Before fracture happens, atoms with high stress concentration and potential energy get rid of the constraint of the crystalline lattice and turn to be dominant. After that, the crystalline phase in the core converts into the disordered state.

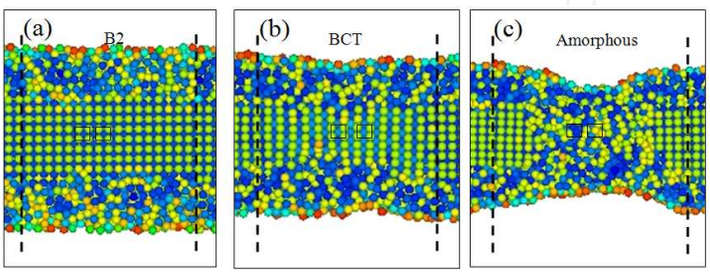

Figure 2. The structural evolution of composite nanowire in stretching, which varies from (a) the B2 state, then (b) the BCT state, to (c) amorphous state.

Only a global description of the structural evolution in the unique core/shell NW during elongation has been provided above, yet extensive analyses on those amazing phenomena are still in great need. To address this issue, three core/shell NW systems containing the same-sized crystalline core (the diameter of the crystalline core is kept at 2 nm) but different size of amorphous surface layer (the crystalline-amorphous ratios are 1 : 1, 1 : 2 and 1 : 3) are analyzed in Fig. 3. As shown in Fig. 3(a), the degree of amorphization has been employed to describe the percentage of the atoms which experiences an order-disorder transformation of the crystalline core inside the system. It is worth noting that the degree of amorphization in the core correlates closely to the crystalline-amorphous ratio. The degree of amorphization in the crystalline core rises from 18% to 40% when the crystalline-amorphous ratio changes from 1 : 1 into 1 : 3, indicating that the degree of amorphization in the core strongly depends on the crystalline-amorphous ratio. Nevertheless, the response between the degree of amorphization in the core and the crystalline-amorphous ratio is nonlinear, which should be discussed in further investigation. The corresponding total strain-stress curves with different crystalline-amorphous ratios are also plotted. As shown in Fig. 3(b), these curves indicate that the ductility of the core/shell NW is proportional to the thickness of the amorphous surface layer whereas the breaking strength keeps declining. In addition, the response of strain energy in crystalline core with strain increasing is also plotted in Fig. 3(c) which can quantitatively reflect the stress concentration exerted by the amorphous surface layer. With the amorphous surface layer thickening, the total strain energy in the crystalline core becomes higher, indicating that a thicker amorphous surface layer could introduce more stress concentration into the crystalline core and thereby convert this zone into a disordered state more easily.

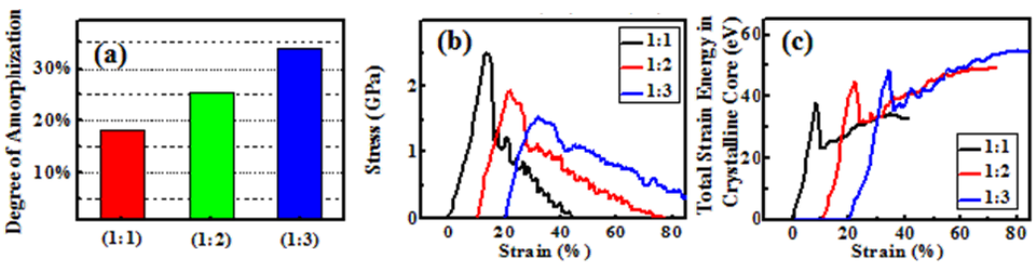

Figure 3. When increasing the surface amorphous thickness, the change curve of (a) the decrystallized degree of the internal crystalline core; (b) the total stress-strain responses; (c) and the strain energy-strain responses of the internal crystalline core. The red and blue curves in (b) and (c) are offset to a strain of 10% and 20%, respectively.

For a better understanding of the corresponding characteristics in the core/shell NW at an atomic level, real-time Honeycutt and Anderson (HA) bond-type index is introduced, which can describe and help to discern the concrete relationships between an atom and its nearest neighbors. The atoms at the high strained region in the crystalline core (ranged from 8 nm to 12 nm) are considered. Figure 4 illustrates the evolution of the BCC bond pairs, as well as the proportion of icosahedral bond pairs in the selected area of crystalline corewith strain increasing, which corresponds to the elongating process shown in Fig. 1. It is noted that when the strain increases, the total amount of BCC type bond pairs (1441 and 1661 bond

pairs) remains approximately constant at first. And then both of them experience a sharp decline from 40% to about 5%. At the same time, the amount of 1541 bond pair which is related to the characteristic of defective icosahedral ordering initially keeps steady and then increases sharply. Moreover, there exists an obvious turning point in both curves which clearly reflects the BCT-disorder transformation corresponding to Fig. 2(c). That is, the BCC bond pairs may firstly convert into the 1541 bond pairs. It should be noted that the increase of the 1551 bond pairs in Fig. 4(b) happens slightly later to that of the 1541 ones. The possible reasons for this special phenomenon will be further discussed in the following.

Further studies focus on the transformation of bond-pairs at the crystalline-amorphous interface and investigate how the local amorphization happen. Figure 5 presents a supercluster consisting of over one hundred atoms taken from the core/shell NW as shown in Fig. 2(b). The red-centered cluster represents the typical BCC lattice, whereas the brown one signifies the icosahedra cluster. At the initial stage, the B2 crystalline core can convert into the BCT structure. Meanwhile, many crystal defects, such as vacancies, can be found near the crystalline-amorphous interface. With the strain increasing, partial atoms near the interface which possess a high potential energy can insert into the crystal defects and consequently result in local amorphization.

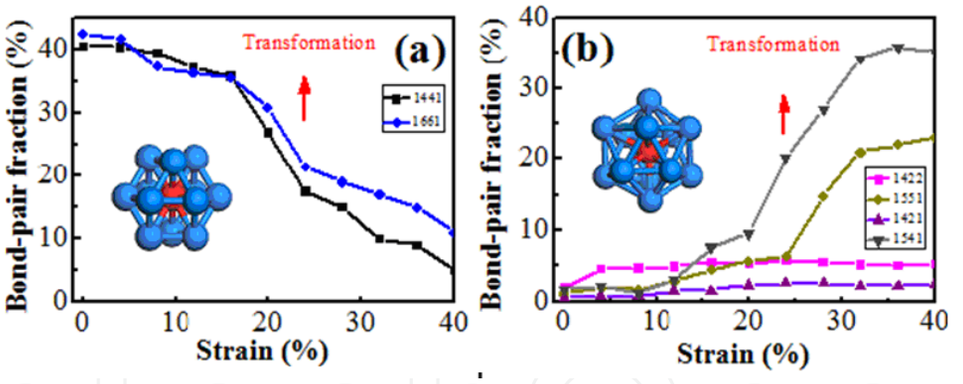

Figure 4. Variation of the main fractions of HA indices in the selected region during stretch process: (a) the decreasing bond pairs; (b) the increasing bond pairs. The insets show the typical B2 and icosahedron structures.

For example, the atom labeled 10 in Fig. 5 can insert into a BCC lattice (the corresponding atoms labels 5, 6, 8 and 9) and form 1541 bond pair. With further elongation, more and more atoms will insert into the crystalline core and the total amount of the 1541 bond pairs becomes larger. It is known that the 1551 polyhedra have a higher resistance to plastic deformation than the 1541 one owing to their higher symmetry. Thus, part of the 1541 bond pairs transforms into the 1551 ones, and as a result, the increase of the 1551 bond pairs is slightly later to that of 1541 ones as shown in fig. 4(b).

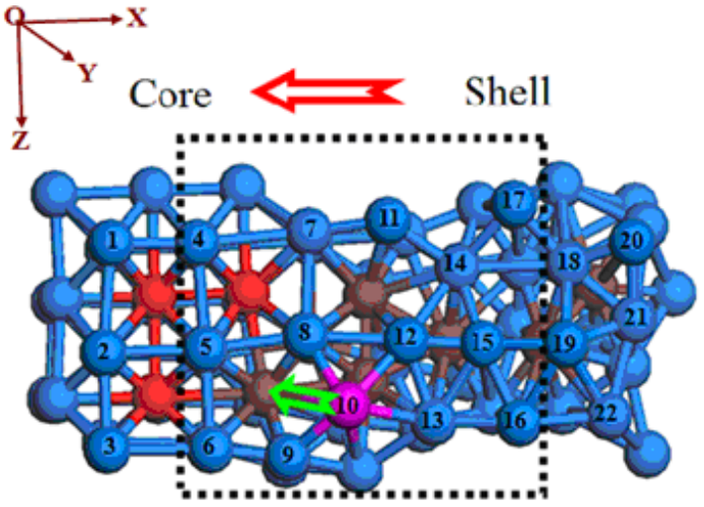

Figure 5. The evolution of bond pairs in the crystalline-amorphous interfaces. For the sake of analysis, atoms in the nearly same plane are shown.

2.4. Strain rate effect on structure of nanowire

Using molecular dynamics simulations with a many-body force field, Ikeda[45] studied the deformation of single crystal Ni and NiCu alloy NWs subjected to uniform strain rates at room temperature. For all strain rates, the Ni NWs is elastic up to 7.5% strain with a yield stress of 5.5 GPa. The crystalline phase transforms continuously to an amorphous phase at high strain rates, exhibiting a dramatic change in atomic short-range order and a near vanishing of the tetragonal shear elastic constant perpendicular to the tensile direction. This phase transformation exhibits a new mode of amorphization[45] or even a super plastic behavior [11]. Higher strain rate may result in deformation twins during plastic deformation as well. As the strain rate decreased to about 0.1% ps^{-1}, a transition of deformation mechanism from combined twining and slip to sequential propagation of slip along well defined and favorably oriented slip plane is observed [11].

2.5. Temperature effect

The mechanical behavior depends highly on the temperature of the system. Several interesting features were observed when the NW was deformed in [001] direction at different temperatures. Due to the higher crystal stability at a lower temperature, the deformation behavior of the NW was characterized by brittle slips, rupture and very low ductility [46]. At the higher temperature of 300 K, the crystal structure became less stable due to higher amplitude of vibration of the atoms about their atomic positions. A relatively stable single-walled helical substructure was formed due to the higher local vibration amplitude of the platinum atoms which enhances the ductility of the NW [46]. The calculated Young's modulus of the NW at T=300K was only about 50% that of bulk platinum, and was significantly smaller than that at T=50K.

2.6. Shape memory

Shape memory is an important property for some engineering materials at large scales. Some NWs also have characteristics of shape memory effect due to structural reorientations which are controlled by a combination of size, thermal energy, and the type of defects formed during inelastic deformation. Certain FCC NWs exhibit both shape memory and pseudoelastic behaviors in atomistic simulations. The formation of defect-free twins and surface stresses is the mechanism that controls the ability of FCC NWs of different materials to show a reversible transition between two crystal orientations during loading and thus shape memory and pseudoelasticity[14].

2.7. Superplasticity

Defect-free Au NWs show superplasticity on tensile deformation [47]. Evidences from high resolution electron microscopes indicated that the plastic deformation proceeds layer-by-layer in an atomically coherent fashion to a long distance. The stress-strain curve provides full interpretation of the deformation. After initial super-elastic deformation, the NW shows superplastic deformation induced by coherent twin propagation, completely reorientating the crystal from <110> to <100>. Uniquely well disciplined and long-propagating atomic movements deduced here are ascribed to the superb crystallinity as well as the radial confinement of the Au NWs. Other mechanical measurements in humid atmospheres suggest that salt NWs also form in ambient environments [48]. Superplastic NWs were formed by touching the NaCl(100) surface with a Au tip in a TEM. The final elongation strain of NWs reached 280%, when showered with the electron beam. More surprisingly, no dislocations were observable during the elongation due to fast diffusion.

2.8. Cold welding

General welding techniques require precise control of the heating mechanism and introduce the possibility of damage. The welding of nano-materials is likely to play an important role in the fabrication of electromechanical nano-devices. The cold welding (a process without heating) on a micrometer scale has been demonstrated, but only at macroscopic length scales and under large applied pressures. Lu et.al [49] demonstrate that single crystalline Au NWs with diameters between 3 and 10 nm can be welded together within seconds by mechanical contact alone, and under relatively low applied pressures. The nearly perfect welding structure possesses the same crystal orientation, strength and electrical conductivity as the rest of the NW. The high quality of the welds is attributed to the nanoscale sample dimensions, oriented-attachment mechanisms and mechanically assisted fast surface-atom diffusion. The cold weld technique is also applied between other kinds of metals such as gold and silver, and silver and silver.

3. Crystalline semiconductor nanowires

3.1. Silicon and silicon compound nanowires

It is generally accepted that Si NWs exhibit linear elastic behavior until fracture without any appreciable plastic deformation. However, the plasticity of Si NWs can be triggered under low strain rate inside the TEM. An electron-beam illuminating with a low current intensity would result in the bond re-forming processes, achieving the plastic deformation with a bent strain over 40% in Si NWs near the room temperature [50]. In some other tensile experiments, the Si NW also showed ultrahigh flexibility and strong toughness [51]. Large strain plasticity (LSP) of single-crystalline Si NWs, which resulted in a fourfold reduction in NW diameter before fracture occurred, was directly observed in an ultrahigh-resolution electron microscope at room temperature. The tensile plasticity was initiated by the emergence of dislocations, followed by the development of a continuous disordered lattice by the emission of dislocations and formation of disordered crystalline structures. The size-dependent fracture mechanism is attributed to the scale-related dislocation activities [52]. For ceramic materials especially at low temperature (~300 K) large strain plasticity of ceramic SiC NWs at nearly room temperature was directly observed in situ by a high-resolution TEM as dimensionality decreases. The continuous plasticity of the SiC NWs[8] is accompanied by a process of increased dislocation density at an early stage, followed by an obvious lattice distortion, which is similar with stretching Si NW.

Individual single-crystalline Si NWs were bent by forming loops or arcs with different radius with high-resolution electron microscopy. Bending-induced ripple buckling was observed and a significant strain variation along the axial direction of the compressive region was revealed. The tensile surface atomic steps and the compressive buckling are the physical origin of the asymmetric tensile-compressive properties of postelastic instabilities and the incipient plasticity. Both of the tensile surface atomic-steps and the compressive buckling initiated versatile ductile plastic dislocation events [53]. Sequential AFM manipulation-scanning protocol is used to observe large bending stress states of [112] Si NWs. It is possible to observe large bending stress states of Si NWs as their radius of curvature is progressively reduced. A slight increase in the fracture strength of Si NWs from 12 to 18 GPa as their radius decreased from 60 to 20 nm was observed in these measurements [54].

The fracture behavior of the Si NWs depends on both temperature and diameter. For NWs of diameter larger than 4 nm, cleavage fracture on the transverse (110) plane favors below the temperature 1000 K. As the temperature increases, the same NWs shear extensively on inclined {111} planes resulting in a brittle-to-ductile transition. As the diameter decreases to less than 4 nm, it fails by shear regardless of temperature. The reason is that the cleavage fracture is initiated by the nucleation of a crack, while shear failure is initiated by the nucleation of a dislocation, both from the surface [55].

Mechanical properties are extremely different at nanometer scale from those at macroscopic scale. Few crystalline nanowires have strength of over 10 GPa, however, Brambilla et al. [56]

have manufactured glass silica nanowires which are characterized by ultimate strength over 10 GPa with a top-down fabrication technique.

3.2. ZnO nanowires

The mechanical properties of ZnO are of considerable interest due to the potential applications in electromechanical devices. These mechanical properties are essential for designing, manufacturing, and operating such devices. ZnO NWs represent excellent model systems to investigate this size dependence, the ability to tune the radius over a continuous range and the manner in which their properties approach those of the bulk as a function of shape and size [57]. Young's modulus of ZnO NWs is essentially independent of diameter and close to the bulk value, whereas the ultimate strength increases for small diameter NWs with values up to 40 times that of bulk [58].

3.2.1. Size effect

A size dependence of Young's modulus in [0001] oriented ZnO NWs (NWs) with diameters ranging from 17 to 550 nm is revealed in Ref. [57]. The measured modulus for NWs with diameters smaller than about 120 nm is increasing dramatically with the decreasing diameters, and is significantly higher than that of the larger ones whose modulus tends to that of bulk ZnO. The radial elastic moduli of [0001]ZnO NWs are determined by contact resonance atomic force microscopy (CR-AFM). The radial indentation modulus and the tangential shear modulus from friction-type measurements are obtained by using realistic tip-nanowire contact geometry. Both moduli increase when the wire diameter is reduced below 80 nm. The size dependence of the elastic properties can be explained by a core-shell model that accounts for a bulk-like core and an elastically stiffer surface layer [59].

Secondly, friction type measurements are useful to directly probe the effects of surface stiffening on the shear response of the NW. Both the lateral shear modulus and radial indentation modulus increase significantly with decreasing NW diameter, which is due to a surface stiffening effect. The results could be understood by the core-shell model of the NW mentioned above, in which the elastic properties of the shell becomes predominant in the limit of small ZnO NW diameters [59].

4. Other novel structures of nanowires

4.1. Ultra thin nanowires

Computer simulations suggest that ultrathin metal wires should develop exotic, noncrystalline stable atomic structures once their diameter decreases below a critical size of the order of a few atomic spacings. The new structures, e.g. helical, spiral-structured wires, whose details depend upon the material and the wire thickness, may be dominated by icosahedral packings. The phenomenon, analogous to the appearance of icosahedral and other noncrystalline shapes in small clusters, can be rationalized in terms of surface energy ani-

sotropy and optimal packing [60]. In some experiments, suspended Au NWs have recently been made in an ultrahigh vacuum and were imaged by the TEM [4]. Mechanisms of formation, evolution, and breaking of these atomically thin Au NWs under stress have attracted great interest.

In some MD simulations, a single chain forms and it is in agreement with experimental results. It shows how defects induce the formation of constrictions that eventually will form the one-atom chains [25]. While in the *Ab initio* calculations, the bond strength of the NW is about twice that of a bulk metallic bond. The importance of knowing bond and atom arrangement is that the total effective stiffness of the nanostructure is strongly affected by them [5].

4.2. Twinned nanowires

Simulation results reveal that with decreasing twin boundary spacing there is a transition from softening to strengthening due to a change in the dominant mechanism of plasticity deformation. Moreover, the value of critical twin boundary spacing is independent of the length of NW but depend on the diameter of the NW. The source controlled deformation mechanism in nanostructured materials will be helpful in understanding the plastic behavior of twinned NWs[61]. Some other simulations reveal the existence of a fundamental limit dividing the mechanical behavior of twinned Au NWs into either strain softening or strain hardening regimes, as a function of the NW diameter and the number of twins. In some other experiments, in-situ tensile testing of Ag NWs with diameters between 34 and 130 nm was carried out inside a SEM. Pronounced strain hardening was observed for most NWs. The strain hardening is mainly attributed to the presence of internal twin boundaries [62]. Since there are size-dependent mechanical properties in NWs, it is necessary for one to develop strategies to control the strength of these materials. The mechanical properties of Ag NWs with a unique fivefold twin structure using a lateral force AFM method were reported by Wu et.al [63]. It exhibits super elastic behavior followed by unexpected brittle failure without significant plastic deformation. However, thermal annealing resulted in a gradual transition to weaker, more ductile materials associated with the elimination of the twinned boundary structure [63].

5. Enhancement of nanowires in nano hybrid systems

The optimized Cu NWs are constrained within the hollow CNT as shown in Fig. 6. It shows the front and side views of the initial configuration of Cu NW encapsulated into CNT(6,6) and CNT(8,8). Bulk copper has a FCC structure. But at nanometer scale, randomly and fully dispersed Cu atoms form a helical or multi-shell equilibrium structure after relaxation to reach the minimum energy. This phenomenon is mainly due to the constraint effect of the template CNT and its special rolled up hexagonal network structure. Cu NW filled in CNT(6,6) (Fig.6(a)) is three-strand NW twisting with each other.

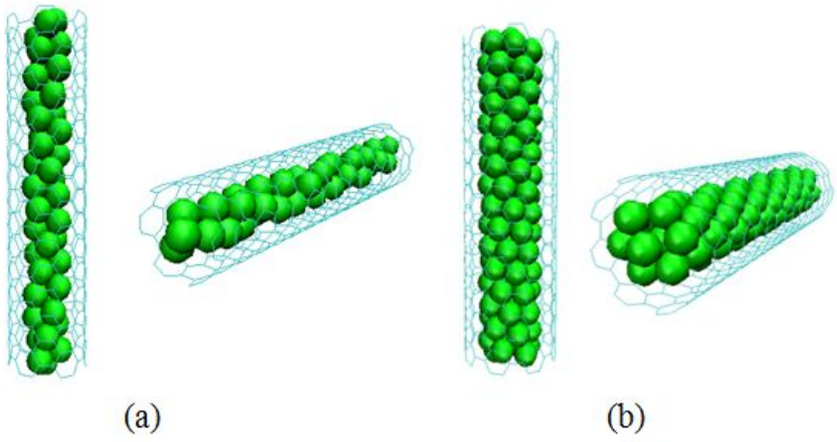

Figure 6. Front and side views of the initial configuration of Cu NW encapsulated in CNT. (a) NW@CNT(6,6), (b)NW@CNT(8,8).

In addition, another Cu NW encapsulated into CNT(8,8) has multi-shell packs that are composed of coaxial cylindrical shells (Fig.6(b)). In this case, Cu NW has a single strand chain at the center. Outside shell is formed by rows of atoms that are helically wound upwards side by side. A displacement increment of 0.0004 nm in axial direction is applied at both ends in each load step. The simulation is carried out at approximately 1 K to avoid thermal effects. Each time step used in the simulation is 1 fs. At the same time, the atoms at both ends of the composite are kept transparent to inter-atomic forces [64].

Figure 7 shows the function of the strain energy of Cu NW@CNT(16,0) with the length of 34.08Å as the time step increases. The inset is a compressive schematic, in which the widths of both fixed ends are 5Å. The constant velocity referred above is imposed on both fixed end atoms which consist of carbon and copper atoms. The strain energy per atom is determined as the difference in total energy per atom of the strained and unstrained NW@CNT. In addition, we use the strain energy of the pristine hollow CNT(16,0) under compressive load for comparison. The strain energy of CNT is increasing non-linearly without any drop before buckling. However, the strain energy of the NW@CNT undergoes a small drop atε=5.2% (Fig.8(b)) and ε=6.6% (Fig. 8(c)) because of slipping of copper atoms during the compressive process. As the strain reaches a critical point at ε=10.4% (t=3000fs), the composite undergoes abrupt buckling deformation resulting in an only 2.7% spontaneous drop which is lower than that of a pristine CNT (33.5%). This means that the composite is more stable than the corresponding pristine CNT when subject to abrupt buckling. Wang et al. [65] have investigated the stability of Ni metal atoms fully encapsulated in CNT. They found that the stability of metal filled in CNT depends much upon the amount of filling metal. When the metal atom is fully filled into CNT, it is more stable than a pristine CNT. This result is similar to some reported in our study. In our calculations, we propose that the mechanical properties of NW@CNTs depend upon the diameter, length, and carbon nanotube's chirality.

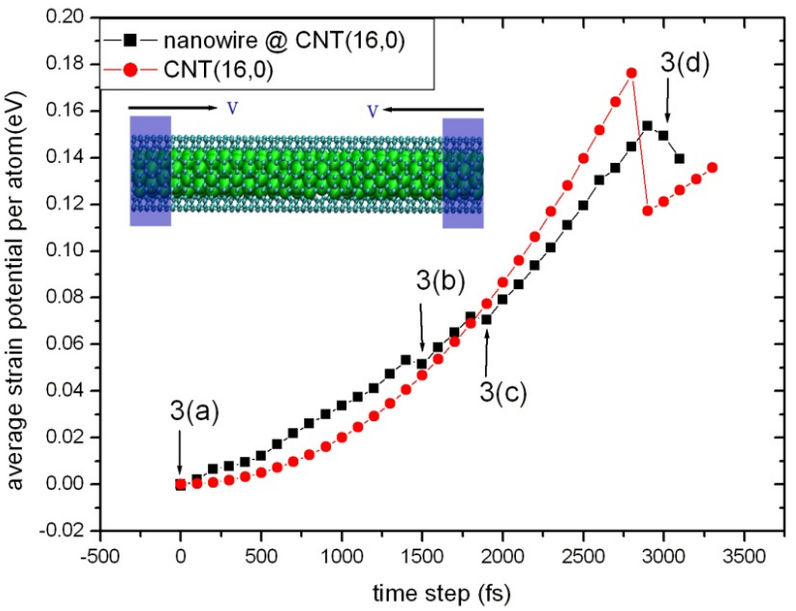

Figure 7. Average strain energy per atom for Cu NW@CNT(16,0) as a function of time step. The red line represents the strain energy of a CNT(16,0) with the same length for comparison.

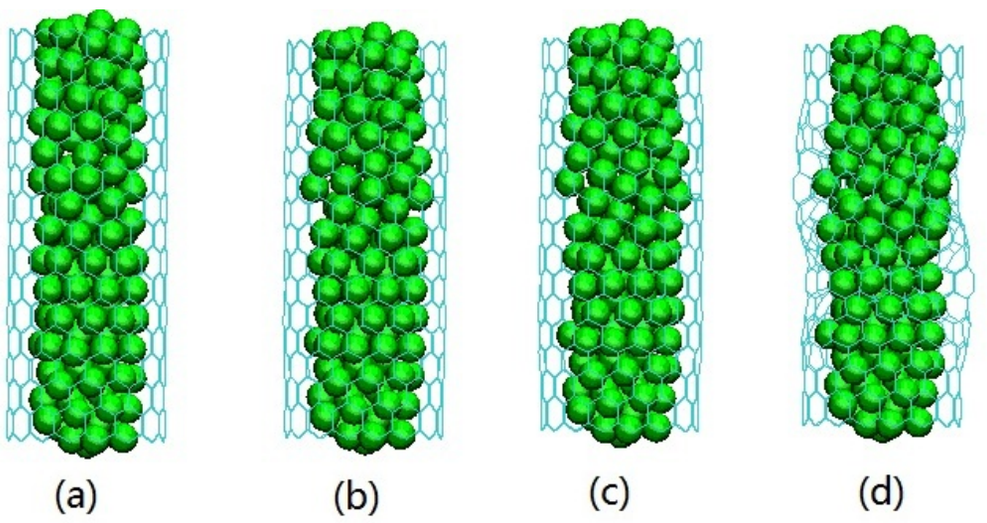

Figure 8. Morphological changes of a Cu NW@CNT(16,0) at different strains corresponding to Fig. 7. (a) Initial configuration. (b) At t=1500fs. (c) At=1900fs. (d) The buckling occurs at t=3000fs.

Table 1 illustrates the relationship between the diameter and buckling loadP_{cr} of a series of Cu NW encapsulated into armchair CNT and zigzag CNT. The lengths of the series of armchair CNTs are approximately 36.9Å, while those of zigzag CNTs are about 34Å.

NWs @armchair carbon nanotubes				
(m,n)	Diameter(Å)	Length/Diameter	Pcr(10^{-7}N)	Increase(%)
(6,6)	8.14	4.53	0.93	-23.7
(8,8)	10.85	3.40	1.28	2.4
(10,10)	13.56	2.72	1.44	14.2
(12,12)	16.27	2.27	1.50	21.9
(14,14)	18.98	1.94	1.65	35.1
(16,16)	21.70	1.70	1.81	45.9
(18,18)	24.41	1.51	2.03	59.8
(20,20)	27.12	1.33	2.29	81.7
NWs @zigzag carbon nanotubes				
(m,n)	Diameter(Å)	Length/Diameter	Pcr(10^{-7}N)	Increase(%)
(10,0)	7.83	4.35	1.12	-12.5
(12,0)	9.39	3.62	1.29	0.7
(14,0)	10.96	3.11	1.30	3.2
(16,0)	12.53	2.72	1.34	7.2
(18,0)	14.09	2.42	1.39	11.2
(20,0)	15.66	2.18	1.41	13.7
(22,0)	17.22	1.98	1.70	39.3
(24,0)	18.79	1.81	1.73	44.2

Table 1. buckling loads P_{cr} for selected Cu NW@armchair CNT and NW@zigzag CNT

When the diameter increases from 8.14 to 27.12 Å (i.e. aspect ratio decreases from 4.53 to 1.33), the buckling load P_{cr} of NW@armchair CNTs increases from 0.93 to 2.29 x10^{-7}N. Moreover, the critical buckling load P_{cr} of NW@zigzag CNTs increases from 1.12 to 1.73 x10^{-7} N as its diameter increases. In order to confirm how the insertion of Cu NW affects the pristine CNT, we calculate the buckling load P_{cr} of NW@CNT in comparison with that of the corresponding pristine CNT. The percentage increase is defined as [(critical buckling load P_{cr} of NW@CNT−P_{cr} of CNT)/P_{cr} of CNT]. As the diameter increases, the percentage increase of both NW@armchair CNTs and NW@zigzag CNTs rises in the same way. Especially for the NW@CNT (20,20) and NW@CNT(24,0), the percentage increase has reached 81.7% and 44.2%, respectively. So the insertion of Cu NW into a thicker CNT reinforces CNT more than the case with a thinner one. Another interesting point we should notice is that when the aspect ratio is 4.53 for NW@CNT(6,6), or 4.35 for NW@CNT(10,0), the percentage increase is minus.

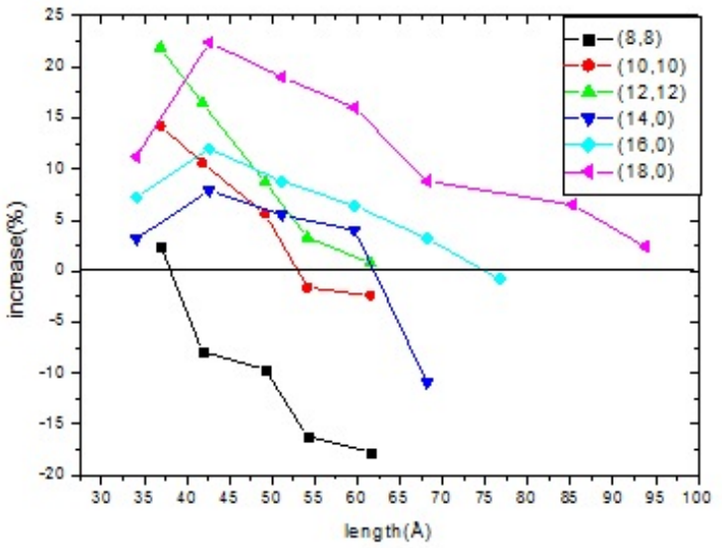

Figure 9. The percentage increase for the buckling loads P_{cr} of the composite material (NW@CNT) compared with the corresponding hollow nanotube.

To further investigate the relationship between length and reinforcing effect of NW@CNT on the critical load, we illustrate the percentage increase of NW@armchair and NW@zigzag CNT as a function of length in Fig. 9. For NW@armchair CNT, the percentage increase decreases as the length increases. There is an equilibrium value for each NW@CNT, after which the percentage increase will be minus. It means that if the length of the NW@CNT is larger than the certain value, the insertion of NW will weaken the strength of CNT. From another point of view, as the length of the composite increases, it can be viewed as one-dimension long column, which means that the stability of the solid column is not stronger than the hollow structure during compression. In continuum mechanics, the Euler formula is employed to determine the critical strain of the long beamlike buckling mode $\varepsilon_{cr} = \frac{\pi^2}{(KL/r)^2}$, where L is the length of the column; $r = \sqrt{I/A}$ is the gyration radius, where I and A are the moment of inertia and the area of cross section; and K is a constant in lieu of the effects of boundary conditions on the Euler formula. The greatest difference between CNT and NW@CNT is the area of cross section. According to the foregoing formula, the critical strain of a solid composite will be smaller than that of the hollow CNT. Furthermore, the buckling load of composite would be smaller than that of CNT.

In other words, when the length of the composite is long enough, Cu NW filled in the CNT buckles earlier than the pristine CNT at a certain strain. There will be some Cu atoms approaching the inside wall of the CNT, resulting in strong interactions along the plane perpendicular to the loading direction. As the compressive strain continues, along with the effect of van der Waals forces included, the interactions between the two different kinds of atoms will initiate the buckling of the whole composite earlier.

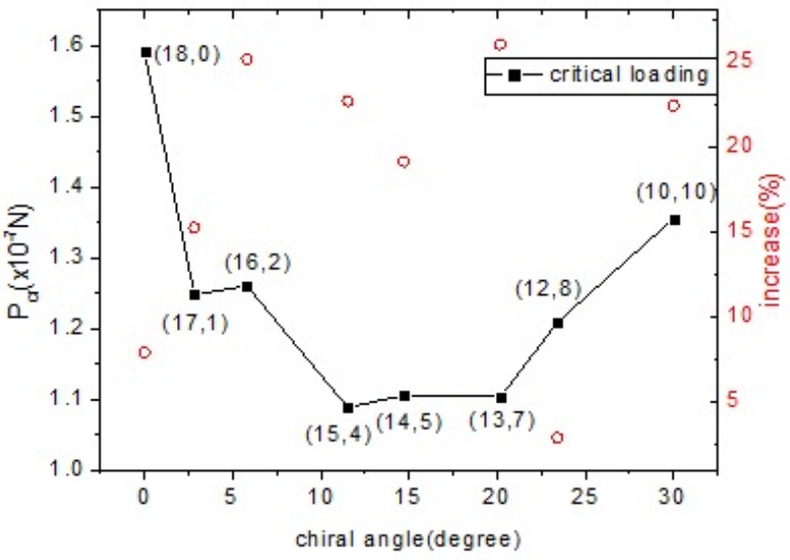

Figure 10. Critical buckling loads (black squares) and the quantity percentage increase of the composite (red circles) with approximately the same diameter and length as function of tube chirality for CNT encapsulating NWs.

Figure 10 shows both the critical loads P_{cr} and the percentage increase as functions of the nanotube's chiral angle. The chirality dependent compressive response of these NWs@CNTs with nearly the same aspect ratio (length=42 Å) is observed. The critical load decreases step-like as the chiral angle increases to about 15° and then increases to 1.36x10^{-7}N when the chiral angle reaches 30 degrees (armchair CNT). The critical load of zigzag CNT encapsulating NWs is the largest of all these types of composites, because there are substantial bonds which are parallel to the loading direction and they can withstand larger compressive loading before buckling. Most chiral CNTs encapsulating NWs are more sensitive than NWs@zigzag CNT in terms of percentage increase. It is seen that copper NWs can increase the critical loading of CNT (13, 7) by about 25%. The insertion of copper NWs into other CNTs with different chiral angles can also enhance the strength of the corresponding pure CNTs. So this enhancement of CNT with different chiral angles makes this kind of composite a promising material to act as building blocks.

In order to further determine the relationship between buckling load P_{cr} and composite's length, the relationship between them is plotted in Fig. 11. Euler formula for the critical buckling load is $P_{cr}=4\pi^2 EI/L^2$, where L is the length. As for NW@armchair CNT with a length ranging from 35 to 65 Å (shown in Fig. 11a), the buckling loads P_{cr} for NW@CNT (8,8) and NW@CNT(10,10) fit nearly linearly with the value $1/L^2$. In addition, the similar trend is also found for NW@CNT (14,0) and NW@CNT(16,0) as shown in Fig. 11 (b).The axial Young's modulus can be defined from the continuum theory in the form of $Y=\frac{d^2E}{Vd\varepsilon^2}$, in which E is the strain energy, ε is the axial strain and V is the overall volume of the whole composite.

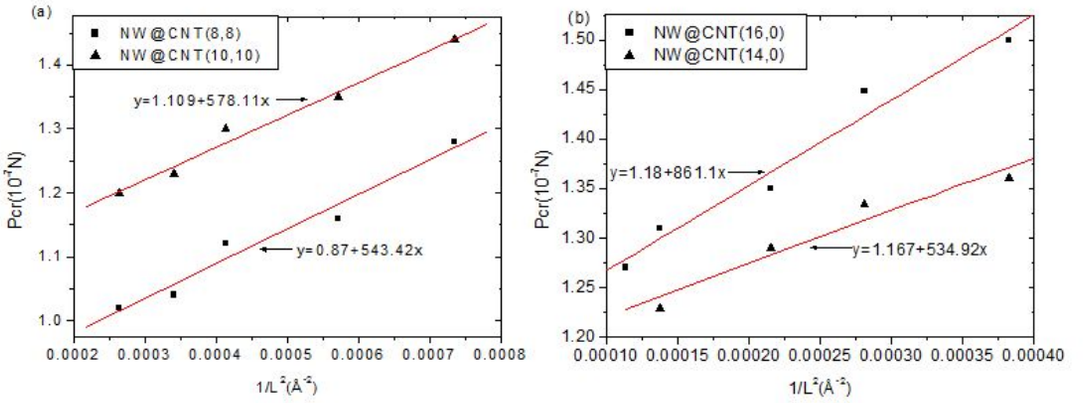

Figure 11. a) Buckling loads P_{cr} of Cu NW@CNT (8,8) and NW@CNT(10,10) verse $1/L^2$ (where L represents the length of NW@CNT), (b) Pcr of Cu NW@CNT(14,0) and NW@CNT(16,0) versus $1/L^2$.

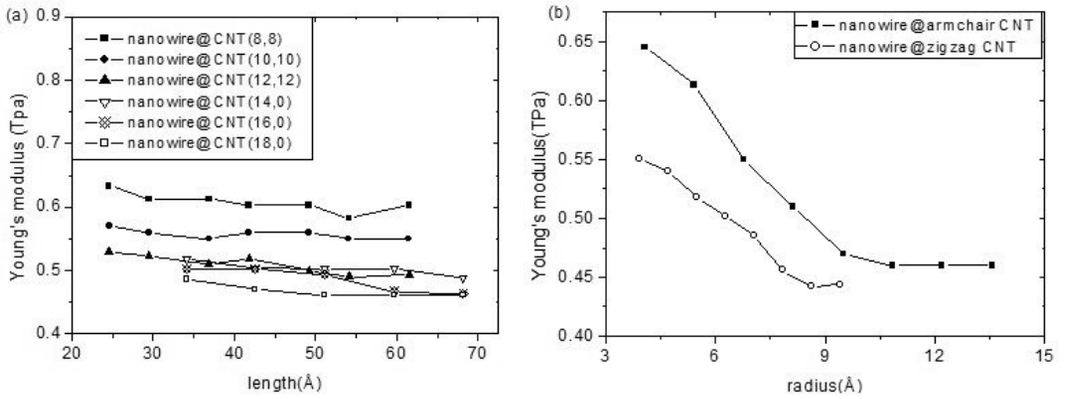

Figure 12. a) Plots depicting the effect of NW@CNT length on the Young's modulus. (b) Plots depicting the effect of NW@CNT radius on the Young's modulus.

As plotted in Fig. 12(a), an increment in length decreases the Young's modulus slightly. A decline of only 4.7% is observed in the decrement of Young's modulus of NW@CNT (8,8) as its length increases from 25 to 65 Å. And there is a similarly small decline of 5.3% in the decrement of Young's modulus of NW@CNT (14, 0) as its length increases from 35 to 70 Å. The general trend is that the Young's modulus decreases as the length of NW@CNT increases. Although there are some points that do not obey this rule, it is mainly due to the different distribution of Cu atoms filled in CNTs. As shown in Fig. 12(b), Young's modulus is sensitive to the radius of NW@CNT ranging from 8 to 14 Å. For example, it drops about 28.7% (i.e. from 0.645 to 0.46Tpa) when radius of the NW@armchair CNT increases from 4.07 to 10.85 Å. In addition, there is a 19.8% drop (from 0.551 to 0.442 TPa) for Young's modulus of NW@zigzag CNT. When the radius is sufficiently large, Young's modulus would reach a constant value 0.46TPa for NW@armchair CNT and 0.44 TPa for NW@zigzag CNT.

6. Conclusions

This paper reviews some recent development on the mechanical properties and mainly focuses on the elongation of a metallic nanowire (NW) with a core/shell structure and the enhancement of helical NWs in a hybrid system.

1. The tensile ductility of the core/shell metallic CuZr NW could be enhanced with the surface amorphous thickness increasing, whereas the breaking strength shows a downtrend instead. During elongation, the NW exhibits three successive deformation stages in crystalline core: lattice distortion, martensitic phase transformation, and local amorphization in the high strained region. Moreover, detailed analysis demonstrates that numerous 1541 bond pairs with defective icosahedral ordering form at first on the weak crystalline-amorphous interfaces. After that, part of them converts into full icosahedral ordering which has the higher resistance to plastic deformation.

2. Dispersed Cu atoms filled in CNT form the novel helical structure after the "simulated annealing" method is carried out. The mechanical properties of this novel composite reveals better than a pristine CNT. The NW@CNTs can withstand larger buckling load than the corresponding CNTs. However, the prerequisite is that the length is smaller than a certain value. On the contrary, when the length is lager than the certain value, the composite could be viewed as a long one dimensional stick; the stability and buckling load would be smaller than that of the corresponding CNT. The critical buckling load also fits linearly well with Euler formula when the aspect ratio of the composite is larger than the certain value. The Young's moduli of NW@CNTs with different diameters have been studied. We find Young's modulus of NW@CNT is more sensitive to its radius than its length. It declines to a constant value as the radius increases.

Acknowledgements

We would like to acknowledge the support from the National Basic Research Program of China (Grant No.2012CB825702). This work is also supported by the National Natural Science Foundation of China (Grant No. 50971081, 51271100). This work is also funded by the grants from Shandong Province in China (Nos. 50625101, ZR2009FM043). We also thank the support from Shandong University (No2009JQ014).

Author details

Hui Li[1*] and Fengwei Sun[2]

*Address all correspondence to: lihuilmy@hotmail.com

1 Key Laboratory for Liquid-Solid Structural Evolution and Processing of Materials, Ministry of Education, Shandong University, China

2 Department of Materials Science and Engineering, Delft University of Technology, The Netherlands

References

[1] Pascual, J. I., Mendez, J., Gomezherrero, J., Baro, A. M., Garcia, N., & Binh, V. T. (1993). Quantum Contact in Gold Nanostructures by Scanning-tunneling-microscopy. *Physical Review Letters*, 71(12), 1852-5.

[2] Agrait, N., Rodrigo, J. G., & Vieira, S. (1993). Conductance Steps and Quantization in Atomic-size Contacts. *Physical Review B*, 47(18), 12345-8.

[3] Olesen, L., Laegsgaard, E., Stensgaard, I., Besenbacher, F., Schiotz, J., Stoltze, P., et al. (1994). Quantized Conductance in an Atom-sized Point-contact. *Physical Review Letters*, 72(14), 2251-4.

[4] Kondo, Y., & Takayanagi, K. (1997). Gold Nanobridge Stabilized by Surface Structure. *Physical Review Letters*, 79, 3455-8.

[5] Rubio-Bollinger, G., Bahn, S., Agraït, N., Jacobsen, K., & Vieira, S. (2001). Mechanical Properties and Formation Mechanisms of a Wire of Single Gold Atoms. *Physical Review Letters*, 87(2), 026101.

[6] Wu, B., Heidelberg, A., & Boland, J. J. (2005). Mechanical properties of ultrahigh-strength gold nanowires. *Nature Materials*, 4(7), 525-9.

[7] Hoffmann, S., Utke, l., Moser, B., Michler, J., Christiansen, S. H., Schmidt, V., et al. (2006). Measurement of the Bending Strength of Vapor-Liquid-Solid Grown Silicon Nanowires. *Nano Letters*, 6, 622-5.

[8] Han, X. D., Zhang, Y. F., Zheng, K., Zhang, X. N., Zhang, Z., Hao, Y. J., et al. (2007). Low-Temperature in Situ Large Strain Plasticity of Ceramic SiC Nanowires and Its Atomic-Scale Mechanism. *Nano Letters*, 7, 452-7.

[9] Chantasiriwan, S., & Milstein, F. (1998). Embedded-atom models of 12 cubic metals incorporating second- and third-order elastic-moduli data. *Physical Review B*, 58(10), 5996-6005.

[10] Branício, P. S., & Rino, P. J. (2000). Large deformation and amorphization of Ni nanowires under uniaxial strain:A molecular dynamics study. *Physical Review B*, 62, 16950-5.

[11] Liang, W., & Zhou, M. (2003). Size and Strain Rate Effects in Tensile Deformation of Cu Nanowires. *Nanotechnology*, 2, 452-5.

[12] Liang, H., Upmanyu, M., & Huang, H. (2005). Size-dependent elasticity of nanowires: Nonlinear effects. *Physical Review B R*, 71, 24, 241403(R).

[13] Lin, S. J., Ju, P. S., & Lee, J. W. (2005). Mechanical behavior of gold nanowires with a multishell helical structure. *Physical Review B*, 72(8), 085448.

[14] Park, H., Gall, K., & Zimmerman, J. (2005). Shape Memory and Pseudoelasticity in Metal Nanowires. *Physical Review Letters*, 95(25), 255504.

[15] Park, H., & Zimmerman, J. (2005). Modeling inelasticity and failure in gold nanowires. *Physical Review B*, 72(5), 054106.

[16] Diao, J., Gall, K., Dunn, M. L., & Zimmerman, J. A. (2006). Atomistic simulations of the yielding of gold nanowires. *Acta Materialia*, 54(3), 643-53.

[17] Ji, C., & Park, H. S. (2006). Geometric effects on the inelastic deformation of metal nanowires. *Applied Physics Letters*, 89(18), 181916.

[18] Baskes, M. I., Angelo, J. E., & Bisson, C. L. (1994). Atomistic Calculations of Composite Interfaces. *Modelling and Simulation in Materials Science and Engineering*, 2(3A), 505-18.

[19] Baskes, M. I. (1992). Modified Embedded-atom Potentials for Cubic Materials and Impurities. *Physical Review B*, 46(5), 2727-42.

[20] Diao, J., Gall, K., & Dunn, M. L. (2003). Surface-stress-induced phase transformation in metal nanowires. *Nature Materials*, 2(10), 656-60.

[21] Stillinger, F. H., & Weber, T. A. (1985). Computer-simulation of Local Order in Condensed Phases of Silicon. *Physical Review B*, 31(8), 5262-71.

[22] Wang, Z. G., Li, J. B., Gao, F., & Weber, W. J. (2010). Tensile and compressive mechanical behavior of twinned silicon carbide nanowires. *Acta Materialia*, 58(6), 1963-71.

[23] Makeev, M., Srivastava, D., & Menon, M. (2006). Silicon carbide nanowires under external loads: An atomistic simulation study. *Physical Review B*, 74(16), 165303.

[24] Mehl, M. J., & Papaconstantopoulos, D. A. (1996). Applications of a tight-binding total-energy method for transition and noble metals: Elastic constants, vacancies, and surfaces of monatomic metals. *Physical Review B*, 54(7), 4519-30.

[25] Da Silva, E., da Silva, A., & Fazzio, A. (2001). How Do Gold Nanowires Break? *Physical Review Letters*, 87(25), 256102.

[26] Da Silva, E., Novaes, F., da Silva, A., & Fazzio, A. (2004). Theoretical study of the formation, evolution, and breaking of gold nanowires. *Physical Review B*, 69(11), 115411.

[27] Park, H. S., Gall, K., & Zimmerman, J. A. (2006). Deformation of FCC nanowires by twinning and slip. *Journal of the Mechanics and Physics of Solids*, 54(9), 1862-81.

[28] McDowell, M. T., Leach, A. M., & Gall, K. (2008). On The Elastic Modulus of Metallic Nanowires. *Nano Letters*, 8, 3613-8.

[29] McDowell, M. T., Leach, A. M., & Gall, K. (2008). Bending and tensile deformation of metallic nanowires. *Modelling and Simulation in Materials Science and Engineering*, 16(4), 045003.

[30] Yun, G., & Park, H. (2009). Surface stress effects on the bending properties of fcc metal nanowires. *Physical Review B*, 79(19), 195421.

[31] Park, H., & Klein, P. (2008). Surface stress effects on the resonant properties of metal nanowires: The importance of finite deformation kinematics and the impact of the residual surface stress. *Journal of the Mechanics and Physics of Solids*, 56(11), 3144-66.

[32] Petrova, H., Perez-Juste, J., Zhang, Z. Y., Zhang, J., Kosel, T., & Hartland, G. V. (2006). Crystal structure dependence of the elastic constants of gold nanorods. *J Mater Chem*, 16(40), 3957-63.

[33] Cuenot, S., Fretigny, C., Demoustier-Champagne, S., & Nysten, B. (2004). Surface tension effect on the mechanical properties of nanomaterials measured by atomic force microscopy. *Physical Review B*, 69(16), 165410.

[34] Jing, G. Y., Duan, H. L., Sun, X. M., Zhang, Z. S., Xu, J., Li, Y. D., et al. (2006). Surface effects on elastic properties of silver nanowires: Contact atomic-force microscopy. *Physical Review B*, 73(23), 235409.

[35] Husain, A., Hone, J., Postma, H. W. C., Huang, X. M. H., Drake, T., Barbic, M., et al. (2003). Nanowire-based very-high-frequency electromechanical resonator. *Applied Physics Letters*, 83(6), 1240-2.

[36] Verbridge, S. S., Shapiro, D. F., Craighead, H. G., & Parpia, J. M. (2007). Macroscopic tuning of nanomechanics: Substrate bending for reversible control of frequency and quality factor of nanostring resonators. *Nano Letters*, 7(6), 1728-35.

[37] Park, H. S. (2006). Stress-Induced Martensitic Phase Transformation in Intermetallic Nickel Aluminum Nanowires. *Nano Letters*, 6(5), 958-62.

[38] Amorim, E., & da, Silva. E. (2008). Helical [110] Gold Nanowires Make Longer Linear Atomic Chains. *Physical Review Letters*, 101(12), 125502.

[39] Zhang, K., Si, P. C., Li, H., Li, Y. F., Yu, H. Q., & Jiang, Y. Y. (2012). Elongation behavior and local amorphization of metallic nanowire with glassy shell and crystalline core. *EPL (Europhysics Letters)*, 97(2), 26005.

[40] Berendsen, H. J. C., Postma, J. P. M., van Gunsteren, W. F., Di Nola, A., & Haak, J. R. (1984). Molecular dynamics with coupling to an external bath. *Journal of Chemical Physics*, 81, 3684.

[41] Allen, M. P., & Tildesley, L. J. (1987). Computer Simulation of Liquids. *(Oxford University Press, Oxford)*.

[42] Wei, Y., Bower, A. F., & Gao, H. (2010). Analytical model and molecular dynamics simulations of the size dependence of flow stress in amorphous intermetallic nanowires at temperatures near the glass transition. *Physical Review B*, 81(12), 125402.

[43] Koh, S. J. A., Lee, H. P., Lu, C., & Cheng, Q. H. (2005). Molecular dynamics simulation of a solid platinum nanowire under uniaxial tensile strain: Temperature and strain-rate effects. *Physical Review B*, 72(8), 085414.

[44] Zhang, K., Si, P. C., Li, H., Li, Y. F., Jiang, Y. Y., Zhang, S. L., et al. (2012). Plastic heterogeneity in nanoscale metallic glass. *Physica E: Low-dimensional Systems and Nanostructures*, 44(7-8), 1461-6.

[45] Ikeda, H., Qi, Y., C¸, agin. T., Samwer, K., Johnson, W. L., & Goddard, I. I. I. W. A. (1999). Strain Rate Induced Amorphization in Metallic Nanowires. *Physical Review Letters*, 82, 2900-3.

[46] Koh, S., Lee, H., Lu, C., & Cheng, Q. (2005). Molecular dynamics simulation of a solid platinum nanowire under uniaxial tensile strain: Temperature and strain-rate effects. *Physical Review B*, 72(8), 085414.

[47] Seo, H. J., Yoo, Y., Park, Y. N., Yoon, W. S., Lee, H., Han, S., et al. (2011). Superplastic Deformation of Defect-Free Au Nanowires via Coherent Twin Propagation. *Nano Letters*, 11(8), 3499-502.

[48] Moore, N. W., Luo, J., Huang, J. Y., Mao, S. X., & Houston, J. E. (2009). Superplastic Nanowires Pulled from the Surface of Common Salt. *Nano Letters*, 9, 2295-9.

[49] Lu, Y., Huang, J. Y., Wang, C., Sun, S., & Lou, J. (2010). Cold welding of ultrathin gold nanowires. *Nature Nanotechnology*, 5, 218-24.

[50] Dai, S., Zhao, J., Xie, L., Cai, Y., Wang, N., & Zhu, J. (2012). Electron-Beam-Induced Elastic-Plastic Transition in Si Nanowires. *Nano Letters*, 12(5), 2379-85.

[51] Hsin, L. C., Mai, W., Gu, Y., Gao, Y., Huang, T. C., Liu, Y., et al. (2008). Elastic Properties and Buckling of Silicon Nanowires. *Advanced Materials*, 20(20), 3919-23.

[52] Han, X. D., Zheng, K., Zhang, Y. F., Zhang, X. N., Zhang, Z., & Wang, Z. L. (2007). Low-Temperature In Situ Large-Strain Plasticity of Silicon Nanowires. *Advanced Materials*, 19(16), 2112-8.

[53] Zheng, K., Han, X., Wang, L., Zhang, Y., Yue, Y., Qin, Y., et al. (2009). Atomic Mechanisms Governing the Elastic Limit and the Incipient Plasticity of Bending Si Nanowires. *Nano Letters*, 9, 2471-6.

[54] Stan, G., Krylyuk, S., Davydov, A. V., Levin, I., & Cook, R. F. (2012). Ultimate Bending Strength of Si Nanowires. *Nano Letters*, 12(5), 2599-604.

[55] Kang, K., & Cai, W. (2010). Size and temperature effects on the fracture mechanisms of silicon nanowires: Molecular dynamics simulations. *International Journal of Plasticity*, 26(9), 1387-401.

[56] Brambilla, G., & Payne, D. N. (2009). The Ultimate Strength of Glass Silica Nanowires. *Nano Letters*, 9, 831-5.

[57] Chen, C., Shi, Y., Zhang, Y., Zhu, J., & Yan, Y. (2006). Size Dependence of Young's Modulus in ZnO Nanowires. *Physical Review Letters*, 96(7), 075505.

[58] Wen, B., Sader, J., & Boland, J. (2008). Mechanical Properties of ZnO Nanowires. *Physical Review Letters*, 101(17), 175502.

[59] Stan, G., Ciobanu, C. V., Parthangal, P. M., & Cook, R. F. (2007). Diameter-Dependent Radial and Tangential Elastic Moduli of ZnO Nanowires. *Nano Letters*, 7, 3691-7.

[60] Gülseren, O., Ercolessi, F., & Tosatti, E. (1998). Noncrystalline Structures of Ultrathin Unsupported Nanowires. *Physical Review Letters*, 80, 3775-8.

[61] Guo, X., & Xia, Y. (2011). Repulsive force vs. source number: Competing mechanisms in the yield of twinned gold nanowires of finite length. *Acta Materialia*, 59(6), 2350-7.

[62] Zhu, Y., Qin, Q., Xu, F., Fan, F., Ding, Y., Zhang, T., et al. (2012). Size effects on elasticity, yielding, and fracture of silver nanowires: In situ experiments. *Physical Review B*, 85(4), 045443.

[63] Wu, B., Heidelberg, A., Boland, J. J., Sader, J. E., Sun, X., & Li, Y. (2006). Microstructure-Hardened Silver Nanowires. *Nano Letters*, 6, 468-72.

[64] Sun, F. W., Li, H., & Liew, K. M. (2010). Compressive mechanical properties of carbon nanotubes encapsulating helical copper nanowires. *Carbon*, 48(5), 1586-91.

[65] Wang, L., Zhang, H. W., Zhang, Z. Q., Zheng, Y. G., & Wang, J. B. (2007). Buckling behaviors of single-walled carbon nanotubes filled with metal atoms. *Applied Physics Letters*, 91(5), 051122.